Early Detection of Invasive *Phragmites australis* at the Tidal Marsh-forest Ecotone with Airborne LiDAR

Biao Xiong [a], Siyuan Han [a], Tyler C. Messerschmidt [b], Matthew L. Kirwan[b], Keryn Gedan [c], Man Qi [d,c*]

[a] *School of Computer Science and Artificial Intelligence, Wuhan University of Technology, 122 Luoshi Rd, Wuhan 430070, PR China*

[b] *Virginia Institute of Marine Science, William & Mary, Gloucester Point, VA, USA*

[c] *Department of Biological Sciences, The George Washington University, Washington, DC, United States*

[d] *Key Laboratory of Geographical Process Analysis and Simulation of Hubei Province, College of Urban and Environmental Sciences, Central China Normal University, Wuhan 430079, China*

1. Abstract

Wetlands across North America are invaded by an introduced lineage of the common reed *Phragmites australis*, and sea level rise has exacerbated the spread of this species. *P. australis* at tidal marsh-forest ecotones has rapidly been expanding into deteriorating forest, colonizing understory environments ahead of native marsh species. Early detection of *P. australis* at the ecotone will be critical to the management of this invasive species in coming decades. In this study, we develop and validate a new method for early detection of *P. australis*, using open access airborne LiDAR data that can uniquely penetrate the tree canopy and detect *P. australis* within the forest understory. The method was designed for areas of sparse to moderate tree cover, such as the forest edge where trees are dying and *P. australis* is expanding, where understory species mapping was previously impossible with most spectral data. To differentiate *P. australis* from shrubs and other understory herbaceous plants, we tested the effectiveness of several LiDAR-derived spatial metrics, including Mean distance, Point density, Scatter, Omnivariance, and Eigentropy, as inputs to a Support Vector Machine (SVM) classifier, followed by a smoothing algorithm to avoid occasional obstacles or disturbances. We

* Corresponding author: manqi@ccnu.edu.cn, Key Laboratory of Geographical Process Analysis and Simulation of Hubei Province, College of Urban and Environmental Sciences, Central China Normal University, Wuhan 430079, China

compare among metrics and single- vs. multiple- metric-based classifications. The resulting best early detection method of *P. australis* achieved a classification accuracy of 91.48% at the development site, and between 56.16% and 80.65% accuracy at other test sites. This algorithm provides a cost-effective and high accuracy method of detecting understory *P. australis* using public airborne LiDAR data. Larger-scale application of this method will provide coastal resource managers and policy-makers with distribution maps of *P. australis* through time in open environments and the forest understory. More generally, this approach provides a framework for mapping understory species and plant functional groups using LiDAR-derived metrics.

Keywords: Species invasion, Understory detection, Sea level rise, Coastal management, Support Vector Machines (SVMs), Lidar-derived spatial metrics.

1. Introduction

An invasive lineage of the common reed, *Phragmites australis*, which originated in Europe and was introduced to North America in the late 1800s, is now a widespread and notorious pest species in the United States (Saltonstall 2002, Saltonstall and Meyerson 2016). The *P. australis* invasion has had strong effects in North- and Mid-Atlantic tidal wetlands, where it forms monocultures that exclude native marsh plants, provides lower quality habitat relative to native marsh species, alters biogeochemistry, and increases sedimentation and accretion (Meyerson et al. 2000, Rooth and Stevenson 2000, Windham 2001). In coastal forests retreating with sea level rise, *P. australis* colonization controls rates of soil elevation change (Langston et al. 2022), and increasing the dissipation of wave energy (Cassalho et al., 2023).

Coastal land managers and property owners identify *P. australis* spread as a primary concern. To combat its negative effects, *P. australis* control programs were developed by public and private conservation organizations. In the USA, over $4 million per year was spent on *P. australis* management and control between 2005 and 2009 (Martin and Blossey 2013). Control methods include application of herbicide, mowing, burning, flooding etc. (Martin and Blossey 2013, Hazelton et al. 2014).

Early detection of *P. australis* is critical for successful control, because *P. australis* is a perennial, rhizomatous, clonal species that quickly forms dense and expansive stands that are difficult to eradicate (Thompson 2003). Throughout the Mid-Atlantic, *P. australis* has not only become dominant in migrating

marshes, but has also spread into forests that are deteriorating in response to sea level rise and saltwater intrusion (Kirwan and Gedan 2019). A study of the Delaware Bay Estuary found that *P. australis* monocultures made up fully half of the historical area of forest retreat (Smith 2013). Field surveys of *P. australis* at marsh-forest ecotones on the Chesapeake Bay Eastern Shore found *P. australis* to be present and well-established underneath forest canopy cover of up to 87.4% (Shaw et al. 2022). Indeed, *P. australis* dominates the biomass and soil properties of the marsh-forest ecotone, even in a system where it has been established for less than 30 years (Langston et al. 2022).

However, it is difficult to detect invasion frontiers of *P. australis* in forest ecosystems. Most marsh plant detections, including prior attempts to map *P. australis* distributions, are based on moderate or high resolution spectral imagery, e.g. Landsat and Worldview (Tian et al. 2020, Zhang et al. 2020, Chen and Kirwan 2022, Anderson et al. 2023, Chen and Shi 2023, Walter and Mondal 2023). Spectral imagery works well in open marsh environments and within canopy gaps of forests (Tian et al 2020, Zhang et al 2020, Chen and Shi 2023) where spectral features of marsh plants are visible. Even some understory vines can be detected using spectral imagery, when they climb tree canopies and become visible to aerial crafts and satellites (Dai et al. 2020). However, for understory species that have no chance to penetrate tree crowns, their spectral features are not captured within traditional imagery, presenting a challenge for remote detection.

To meet this challenge, Light Detection and Ranging (LiDAR) has proved effective in detecting forest canopy structure and identifying understory vegetation (Lines et al. 2022, Jucker et al. 2023, Kostensalo et al. 2023). LiDAR is an active remote sensing method that uses light in the form of a pulsed laser to measure variable distances to Earth. These light pulses, combined with other data recorded by the airborne system, generate precise, 3D information about the shape of the Earth and its surface characteristics. In forests, laser pulses can penetrate minute canopy gaps to reach understory layers and provide information on multiple canopy layers (Sumnall et al. 2021).

In recent years, LiDAR data has been increasingly applied to detect subcanopy forest elements (Lines et al. 2022). For example, presence or absence of understory vegetation was discriminated using a bimodal canopy height profile or symmetrical structure of the trees from airborne LiDAR (Melo et al. 2021, Huo et al. 2022). Leaf area index and forest productivity have been estimated using integrated laser energy, backscattering coefficients, leaf scattering, and the light penetration index (Song et al. 2021, Sumnall et al. 2021). Combinations of terrestrial and airborne LiDAR, as well as unmanned aerial vehicle-born LiDAR and

hyperspectral fusion have been employed to estimate understory biomass, using metrics such as mean canopy height, diameter at breast height, wood density, canopy cover, vegetation volume, and cross-sectional area of stems (Bazezew et al. 2021, de Almeida et al. 2021, Li et al. 2021). In another application, understory vegetation density and cover was predicted by dividing the point cloud into multiple layers according to different heights and calculated the metrics at different height ranges (Latifi et al. 2016, Campbell et al. 2018, Venier et al. 2019).

Several studies have attempted to identify subcanopy functional groups or differentiate species. For example, Latifi et al. (2017) tried to identify different understory plant functional groups (shrubs, herbs, and mosses) using a thinning algorithm and achieved a coefficient of determination (R^2) varying from 0.48 to 0.80. Gopalakrishnan et al. (2018) quantified understory layer canopy density, as the ratio of LiDAR returns in the understory to those near the ground, and found that this was the most important predictor for understory shrub detection, using this parameter to achieve 62% accuracy in detecting understory shrubs. Hakkenberg et al. (2018) used a multi-scale nested vegetation sampling in conjunction with LiDAR-hyperspectral remotely sensed data to map vascular plant species turnover in a diverse and structurally complex forest. Singh et al. (2015) applied LiDAR and spectral data to detect the spatial distribution of the exotic understory plant *Ligustrum sinense*, a rapidly spreading invader in the urbanizing region of Charlotte, North Carolina, USA, and achieved a maximum accuracy of 69.9% with the random forest model. Together, these works demonstrate the potential to use LIDAR to map the distribution of invasive species in the understory of coastal forests.

The objective of this study was to detect subcanopy *P. australis* in the climate change-sensitive marsh-forest ecotone of Maryland and Virginia using airborne LiDAR. Unlike previous LiDAR-based studies that extract understory information using variables, such as return number or intensity, that are only accessible from full-waveform LiDAR data (Torralba et al. 2018), we propose to use the spatial distribution of LiDAR points to construct species-specific metrics for our target species. A specialized method is warranted because the 3D structure information within the point cloud can record a plant stands' morphological characteristics, determined by shape, size, and density of leaves, length, and thickness of branches etc. Therefore, a particular species can be detected with carefully designed metrics that reflect their unique point cloud characteristics. For *P. australis*, in particular, its upright and dense stems and leaves as well as spatially continuous canopy height make it distinctive from other co-occurring plants. Secondly, although the return information from

LiDAR is an important metric, not all LiDAR data are full-waveform, and public datasets often omit full-waveform data. The spatial distribution information of the point cloud of LiDAR data is more widely available and provides a high-quality source of information.

To detect subcanopy *P. australis* at the forest-marsh ecotone, we firstly identified key spatial features of the LiDAR point cloud, namely point distance, point density, scatter, omnivariance, and eigentrophy, that were sensitive to the morphological characteristics of plant stands within our study region. Then, we tested and fine-tuned the SVM algorithm to detect *P. australis*, followed by a smoothing algorithm to optimize the detection results. We hope that the classification framework we propose will not only pave an efficient avenue for *P. australis* mapping where a forest canopy is present, but also provide a new application for LiDAR-based understory vegetation monitoring at the species level and enhance our understanding of vegetation dynamics in changing forest.

2. Material and methods

2.1.Study area

We selected nine sites on the Delmarva Peninsula, USA (Fig. 1) to ground truth the presence or absence of *P. australis* for training and validation of the classification algorithm. In the region, *P. australis* is a key species in the response of tidal marsh to accelerating sea level rise, and it has become dominant in migrating marshes, spreading into dead and dying forests (Shaw et al. 2022). Co-occurring understory species in the forest-marsh ecotone community include the shrubs *Morella cerifera, Baccharis halimifolia,* and *Iva frutescens,* native marsh grasses *Spartina patens* and *Distichlis spicata,* and upland grasses such as *Panicum virgatum* and *Chasmanthium laxum* (Gedan and Fernández-Pascual 2019, Kearney et al. 2019, Kottler and Gedan 2020, Sward et al. 2023). We selected The Nature Conservancy's Brownsville Preserve in Nassawadox, Virginia as a site to train and validate the classifier, and we used data from the eight other sites to validate the robustness of the classifier.

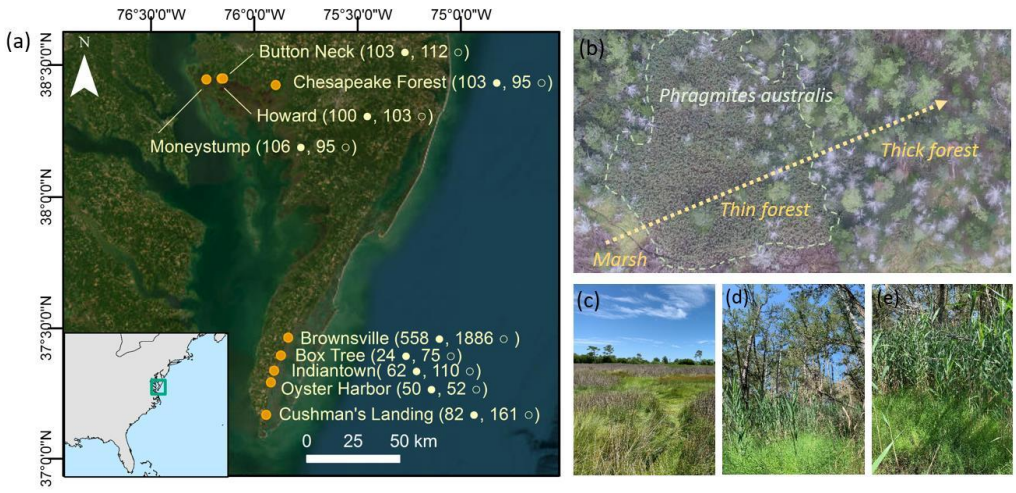

Fig. 1. Nine study sites in coastal Maryland and Virginia, USA (green box in inset). (a) shows the field sites where *P. australis* detection algorithm was trained and calibrated. Number in bracket showed the number of positive samples (●) and negative samples (○) at each study site. (b) is a drone image of the marsh-forest ecotone in Brownsville, typical of the region and invaded by *P. australis* (dashed green line), (c) photo of open marsh where presence/absence of *P. australis* is easily detected within drone imagery, (d) and (e) show the establishment of *P. australis* in thin and thick forest, respectively, where detection of *P. australis* is obscured by the tree canopy in spectral imagery.

2.2.Data acquisition

Open access airborne LiDAR data (Fig. 2a) released by USGS (https://apps.nationalmap.gov/downloader/#/) was used to detect *P. australis*. The LiDAR data for sites at Virginia (i.e., Brownsville, Box Tree, Indiantown, Oyster Harbor and Cushman's Landing sites) were collected in April 2015, with a point spacing of 0.38~0.45 m and up to seven returns and intensity values for each point. The LiDAR data for sites at Maryland (i.e., Button Neck, Chesapeake Forest, Howard, and Money Stump) were collected between December 2013 and April 2014, with a point spacing of 0.47~0.50 m and up to five returns and intensity values recorded for each point.

Tidal Marsh Vegetation Community Classification (https://nalcc.databasin.org/datasets/6a64b843c61e41688091d75bd1718fc0/) is a map product developed by North Atlantic Landscape Conservation Cooperative (NALCC) that provides a continuous classification of tidal marsh cover types in the Northeast Atlantic coast at a resolution of three meters. This map is produced

with remote sensing using 2014-2015 National Agriculture Imagery Program (NAIP) multispectral imagery and National Elevation Dataset. Notably, compared with other tidal wetland mapping products, e.g., National Wetland Inventory (Wilen and Bates 1995, https://fwsprimary.wim.usgs.gov/wetlands/apps/wetlands-mapper/), this map stands as the sole large-scale mapping resource delineating the distribution of *P. australis* on marshes with an overall classification accuracy *of 75%.* However, due to the limitation of NAIP data and small amount of training data, the NALCC classification cannot accurately distinguish *P. australis* near the forested, terrestrial border. In Fig. 2 (c), the NALCC map of Brownsville displays a conspicuous absence of *P. australis* in the terrestrial area, starkly contrasting with our field survey results that reveal a significant invasion within the same region. Consequently, to establish reliable ground truth data, we conducted both field surveys and drone assessments.

Ground truth observations of *P. australis* presence and absence at Brownsville Preserve were collected from ground surveys in August 2019 and from visual interpretation of drone images collected in September 2019 (Fig. 2b). Specifically, ground surveys were conducted in 24 plots (20 × 20 m each) spanning across a gradient tree canopy openness. In each plot, a density category of *P. australis* (*i.e.*, absence – 0 stem, low-1~3 stem, medium - small group of stems, high - sparse stand, highest - fully developed stand) was recorded in a 5 m grid (dots in Fig. 2b). A handheld Garmin eTrex 32X GPS was used to geolocate a corner of each plot, and transect tapes and a compass were used to maintain grid spacing across each plot (dots in Fig. 2b). At a slightly larger scale, the distribution of *P. australis* in open marsh and deteriorating forest was visually interpreted within drone imagery, in which *P. australis* can be distinguished by its distinctive textural feature (Appendix A: Table A1). Drone images were collected with a DJI Mavic flying at 120 m aboveground in September 2019 when *P. australis* exhibits peak biomass and prior to fall senescence. The drone images had a horizontal accuracy of around 4 m and a spatial resolution of 5.6 cm. Consequently, at Brownsville we acquired a total of 2470 samples as ground truth value, of which 584 were positive samples with *P. australis* present (54 in the marsh and the rest in the forest) and 1886 were negative samples with *P. australis* absent (781 in the marsh and the remainder in the forest).

To validate the robustness of the classification algorithm, extra validation samples were collected (Fig. 1) at Box Tree (24 positive samples, 75 negative samples), Indiantown (62 positive, 110 negative), Oyster Harbor (50 positive, 52 negative), Cushman's Landing (83 positive, 161 negative), Button Neck (103 positive, 112 negative), Chesapeake Forest (103 positive, 95 negative), Howard (100 positive, 103 negative), and

Moneystump (106 positive, 95 negative) in September 2022. Validation samples of sites in Maryland were collected with ground surveys. Validation samples of sites in Virginia were collected using a combination of drone and ground surveys. Ground surveys of these additional validation samples were conducted along trails that cut across forest-marsh boundaries. Along the trail, density of *P. australis* was recorded every 10 meters with a handheld Garmin eTrex 32X GPS. Drones images were collected with the same drone model and data quality to that of Brownsville, and were visually interpreted following the same protocol as at Brownsville.

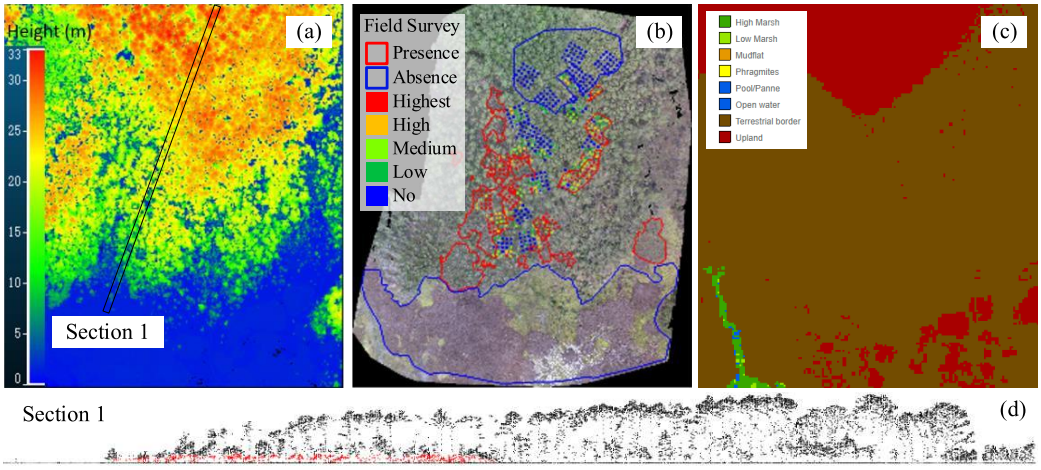

Fig. 2. *P. australis* map of Brownsville Preserve area. (a) Airborne LiDAR with color coded by maximum return height; (b) The distribution of ground truth samples of *P. australis* presence or absence. Polygons in panel **b** represent aerial-based ground truth data (blue - *P. australis* absent, red - *P. australis* present). For ground surveys (dots), blue represents *P. australis* absence; dots in dark green, light green, yellow, and red represent *P. australis* presence at low (1~3 stem), medium (small group of stems), high (sparse stand) and highest (fully developed stand) density following Sward et al. (2023). (c) NALCC dataset with *P. australis* mapped in yellow (detected in several pixels within marsh area in the bottom left corner of the scene); (d) Side view of section 1 in (a), the red dots present *P. australis*.

2.3 Classification framework

The *P. australis* detection algorithms consist of three steps: data pre-processing, metric selection, and classification and optimization (Fig. 3).

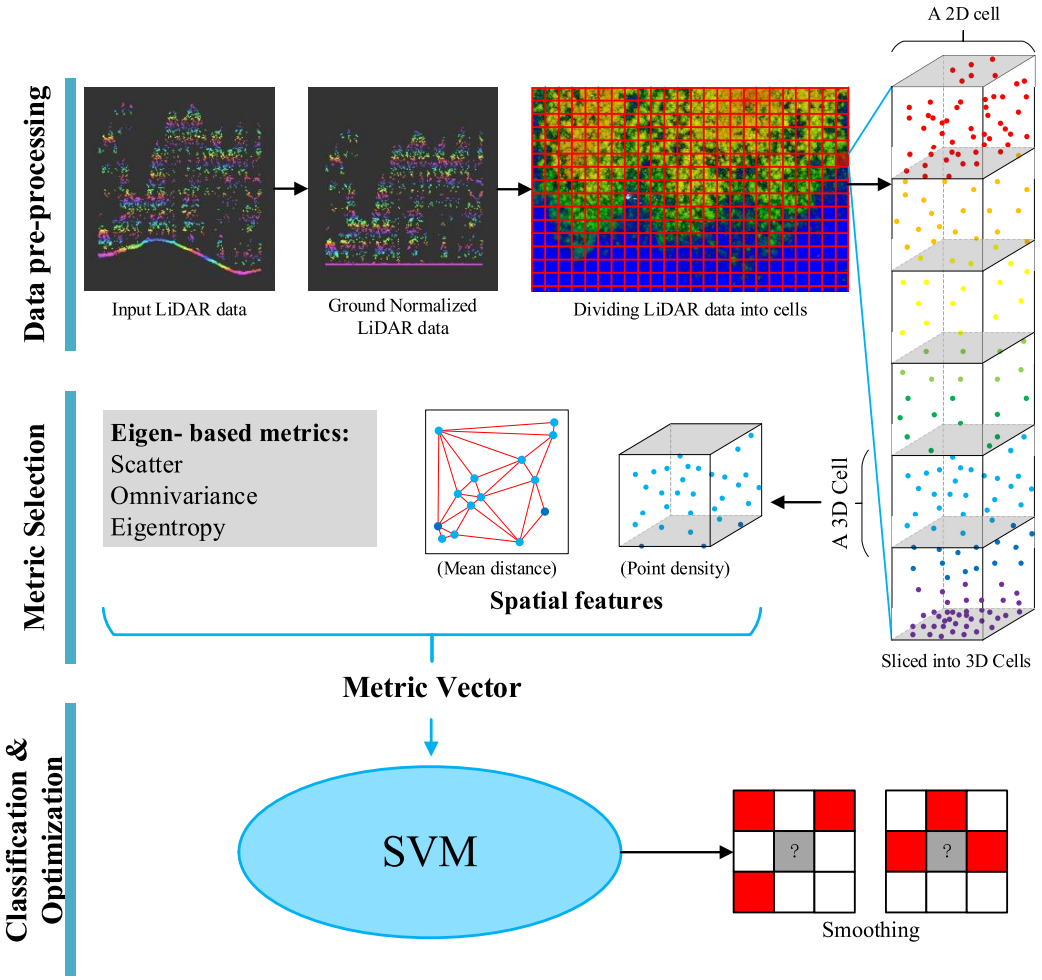

Fig. 3. The pipeline of the proposed classification algorithm. The input lidar data is normalized with respect to the ground surface, and subsequently divided into 3D cells. Within each 3D cell, point features are computed and then projected onto the 2D cell situated on the X-Y plane. The resulting point features for each 2D cell are then fed into a Support Vector Machine (SVM) classifier, responsible for labeling each cell as either *P. australis* present or not. A smoothing algorithm is then used to refine the classification output based on the relationships among neighboring cells.

Data pre-processing

We generated a Normalized Digital Surface Model (N-DSM) to exclude ground elevation from LiDAR point height (Datum: NAD1983) following a TIN densification algorithm (Axelsson 2000), in order to acquire height of points relative to the land surface. We then rasterized LiDAR data into 5 × 5 m grids to match the resolution and coordinates of ground surveyed points (Fig. 3).

To discard redundant point clouds from upper canopies, we limited the height of each 5 × 5 m grid to 8

meters from the surface, which exceeds the height range of *P. australis* (2 - 4 m in height). We then horizontally sliced the grid into multiple layers with a designated height step (Fig. 3), and calculated the spatial distribution features of the point cloud within each slice as representatives of morphological characteristics of *P. australis* stands. The height steps (***h***) tested ranged from 0.1 m to 1.5 m with an interval of 0.1 m to identify the optimal height step corresponding to the highest classification accuracy.

Point Features

To represent the spatial distribution characteristics of point cloud within each 3D cell effectively, we have carefully selected five metrics: *Density (D), Mean Distance (M), Scatter (S), Omnivariance (O) and Eigentropy (E)*.

Point density is defined as the ratio of Lidar points to the volume of a 3D cell (points per m^3). Mean distance is defined as the average distance between points projected onto the X-Y plane and is calculated with Triangulated Irregular Network (TIN) model (Fig. 3). Scatter (S), Omnivariance (O) and Eigentropy (E) are computed based on the three eigenvalues (λ_1, λ_2, λ_3) of the covariance matrix for all points within each 3D grid following Karen et al. (2004). The three Eigen-based metri cs are defined as below:

$$Scatter = \lambda_3/\lambda_1 \quad \text{Eq. (1)}$$

$$Omnivariance = \sqrt[3]{\lambda_1\lambda_2\lambda_3} \quad \text{Eq. (2)}$$

$$Eigentropy = -\lambda_1 \log(\lambda_1) - \lambda_2 \log(\lambda_2) - \lambda_3 \log(\lambda_3) \quad \text{Eq. (3)}$$

where $\lambda_1 \geq \lambda_2 \geq \lambda_3$.

We normalize all the point features within the range of 0 to 1 before feeding them into the SVM classifier. Subsequently, the features of all 3D cells sharing the same X-Y position are consolidated into a single point feature denoted as $F = (f_1, f_2, \ldots, f_n)$, where n corresponds to the number of vertical slices. These features are categorized into distinct feature vectors, namely F^D, F^M, F^S, F^O, and F^E.

Classification

In our approach, we have selected Support Vector Machines (SVMs) as the binary classifier to tackle our *P. australis* classification problem because of its strength in classifying relatively small sample datasets with high-dimensional feature spaces (Cortes and Vapnik 1995), and its generalization and robustness to new, unseen data (Hartling et al. 2019, Kattenborn et al. 2021). After testing different kernel functions, such as Linear, Sigmoid, CH2, and Histogram Intersection kernels, we found the Radial Basis Function to be the

most suitable kernel for our specific classification task.

Smoothing

Considering the way that *P. australis* tends to expand mostly through clonal spread (Kettenring et al. 2016), resulting in paths that often exceed the grid size (5 m) used in the classification process and exhibit lateral continuity in marsh and under trees. We decided to take context information into account, so misclassification caused by occasional obstacles or disturbances such as shrubs or tree trunks can be corrected by contextual information.

To achieve this, we designed a slicing window as the convolution kernel to convolve with the label image. The 3 × 3 slicing window is shown in Fig. 4, where the four corners are weighted $\sqrt{2}/2$, and the others are weighted 1, which is the inverse of their distance from the target grid. Unlike the standard Gaussian kernel, our proposed kernel assigns equal weights to the center and its left, right, up, and bottom neighbors (Fig. 4).

$\frac{\sqrt{2}}{2}$	1	$\frac{\sqrt{2}}{2}$
1	1	1
$\frac{\sqrt{2}}{2}$	1	$\frac{\sqrt{2}}{2}$

Fig. 4. The proposed smoothing kernel.

The status of smoothed image can be calculated as

$$\tilde{I} \approx \frac{\sum_1^9 \omega_i I_i}{\sum_1^9 \omega_i} \quad \text{Eq. (4)}$$

where the input image I is a Binary image, the value 0 and 1 indicates the presence and absence of *P. australis*. The smoothed image $\tilde{I}$ is also a binary image by rounding the convoluted values. If needed, the smoothing operation can be applied multiple times to incorporate an increasing amount of contextual information, further refining the detection of *P. australis*.

3. Experiments and Results

We tested the sensitivity of the classification result to different parameter combinations to optimize the classification algorithm. The parameter combination we tested includes *height step*, *feature combination*, and

smoothing rounds. For each parameter optimization, we used ground truth data collected from Brownsville to optimize and validate the classification algorithm. The training samples take up 70% of ground truth data validation samples take 30% of ground truth data if not specifically defined. We repeated the entire training and testing pipeline 50 times to calculate the mean classification accuracy.

We use the three most used metrics to evaluate the classification accuracy -- Accuracy, Recall, and F_1-score -- to estimate the performance of combined feature. Accuracy measures the proportion of correctly classified instances out of the total number of instances in the dataset. Recall measures the proportion of true positive predictions out of all actual positive instances and focuses on the ability to find all positive instances. While F1-score provides a balanced measure of both precision and recall, as defined as follows:

$$Accuracy = (TP + TN)/(TP + TN + FP + FN) \quad \text{Eq. (5)}$$

$$Recall = TP/(TP + FP) \quad \text{Eq. (6)}$$

$$F_1 = 2TP/(2TP + FP + FN) \quad \text{Eq. (7)}$$

where TP is the sample number of True Positive, TN is the sample number of True Negatives, FP is the sample number of False Positives, FN is the sample number of False Negatives.

3.1.Optimal height step

For *height step*, we used a single-feature-based classifier to identify the optional height step for each feature. We tested all the five individual features (D – Density, M – Mean Distance, S – Scatter, O – Omnivariance, and E – Eigentropy) with five classifiers. For each classifier, we test the variation of classification accuracy in response to changes in the height step (0.1~1.5 m, with 0.1 m interval).

The sensitivity of classification accuracy to the height step parameter indicated each metric has its own optimal height step (Fig. 5), reflecting the unique information captured by the features. The best classification was achieved by Mean distance (M) at 87.16% accuracy with a height step of 0.3 m, followed by Eigentropy (85.56%) with a step of 0.5 m, Omnivariance (83.37%) with a step of 1.5 m, Scatter (77.96%) with a step of 1.5 m, and Density (76.76%) with a step of 1.0 m.

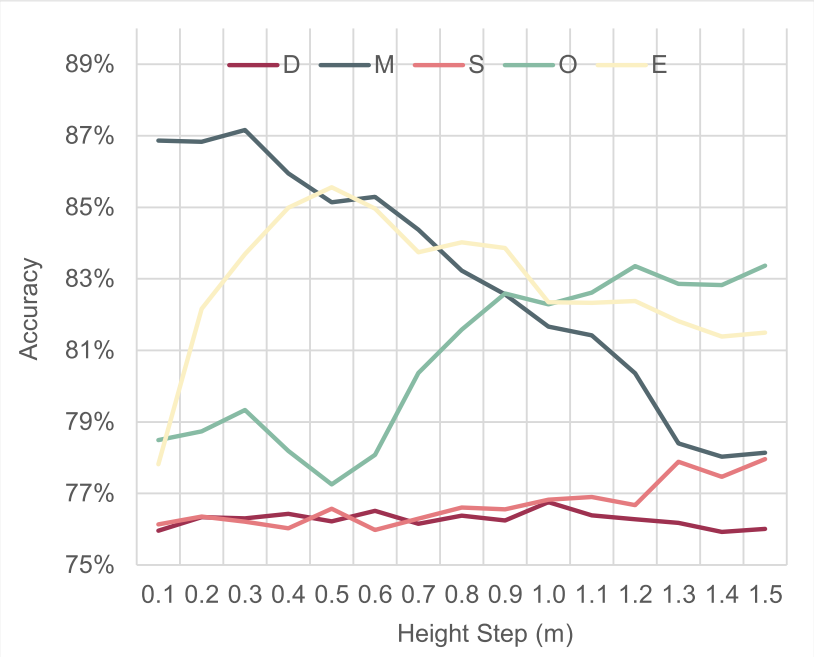

Fig. 5. The classification accuracy using various height steps for all point metrics, including *Density (D), Mean distance (M), Scatter (S), Omnivariance (O) and Eigentropy (E)*.

3.2.Feature combination

For *feature combination*, we tested whether using a combination of different features can greatly improve classification accuracy compared with using singular feather. Though different features might have their own optimal height steps, to simplify the analysis, we select the height step (0.5 m) which worked well for all point features. Features are ranked according to their classification accuracy performance in that height step. If the ranking order is O, M, E, D, S, Ominivariance has the highest classification accuracy, then Mean distance, and so on. We enriched the feature combination by gradually adding lower performing features into the combination, e.g. OM, OME, OMED, OMEDS. Here OM stands for a combination of Omnivariance and Mean Distance, which is fulfilled by stacking feature vector O and M into one feature vector.

As depicted in Fig. 6, the combination of Omnivariance and Mean Distance (i.e. OM) achieved the highest Accuracy (84.92%) and Recall (74.22%), though F1-score (63.12%) was slightly lower than the peak (64.56% under singular feature Omnivariance). When more features were included in the combination, classification results deteriorated.

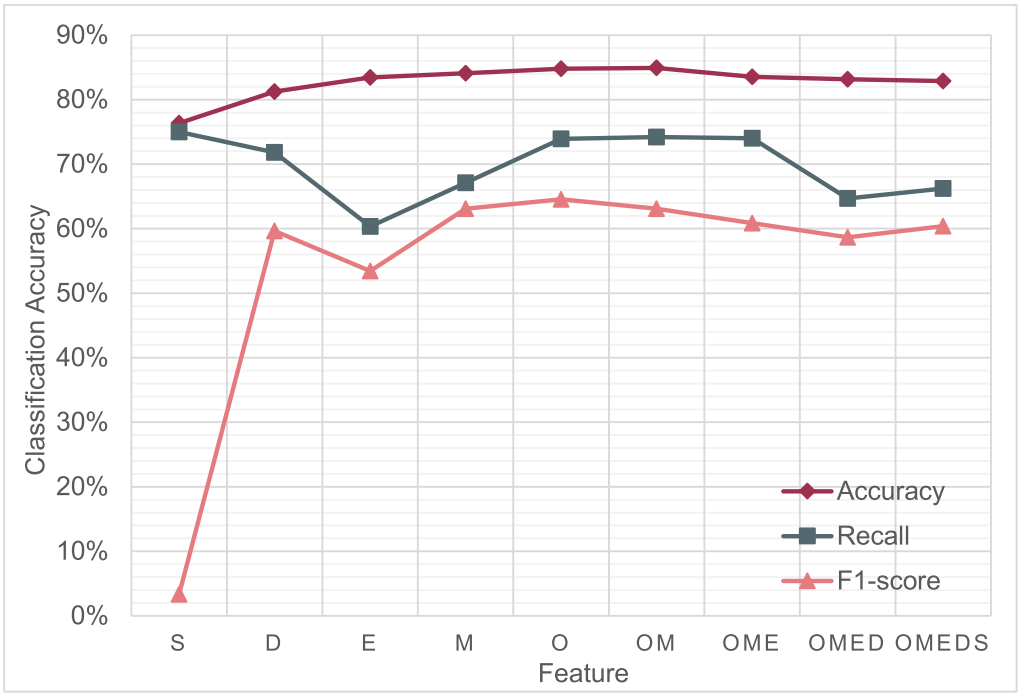

Fig. 6. The classification accuracy on Brownsville dataset with individual or combination of point features. D – Density, M – Mean Distance, S – Scatter, O – Omnivariance, and E – Eigentropy.

3.3.Optimization by Smoothing

For *smoothing*, we assessed the efficacy of smoothing operations in improving the accuracy of *P. australis* detection. Combined features of Omnivariance and Mean Distance, i.e. OM, at 0.5 m height step was selected to generate a *P. australis* distribution map. Subsequently, we investigated the impact of multiple rounds of smoothing operations on the classification accuracy.

The results revealed a gradual increase in Accuracy, Recall, and F1-Score with the first three or four rounds of smoothing, followed by slightly decrease with extra round (Fig. 7). Accuracy increased from 88.78% to 91.48%, and F1-score increased from 74.47% to 80.11% after four rounds of smoothing, Recall increased from 70.35% to 73.86 after three rounds of smoothing. After five rounds of smoothing, Accuracy, Recall and F1-score decrease to 91.11%, 73.51%,79.36%.

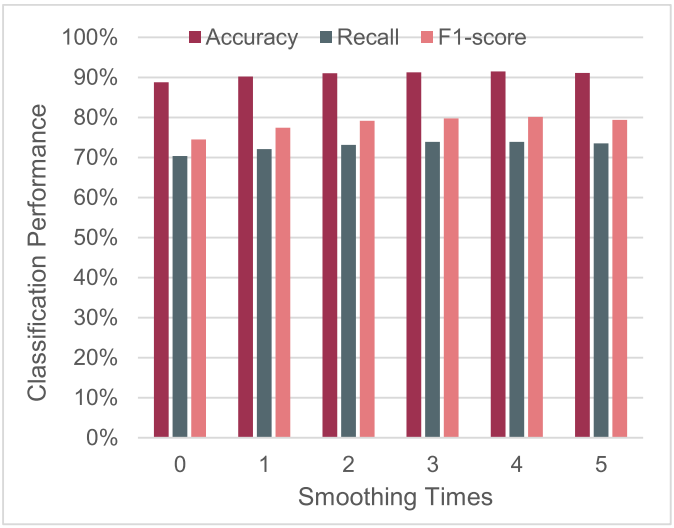

Fig. 7. Detection accuracy with varying rounds of smoothing operations.

Fig. 8 depicts the impact of smoothing on the predicted distribution of *P. australis* in rownsville. The field survey results are color-coded, with cyan and blue denoting the presence and absence of *P. australis*, respectively. Meanwhile, in the classification results, red signifies *P. australis* presence, green represents its absence, and grey denotes bare ground or short stature vegetation (counted as the absence of *P. australis*). The image reveals the merging of small regions with their larger neighboring areas, including both heavily-invaded and uninvaded areas. Notably, the erroneous detection of *P. australis* in the blue regions (Fig. 8a) was effectively rectified and removed by smoothing. These regions consisted of isolated small sections with one to three pixels. The smoothing process aligns with the knowledge that *P. australis* typically does not grow in small clumps.

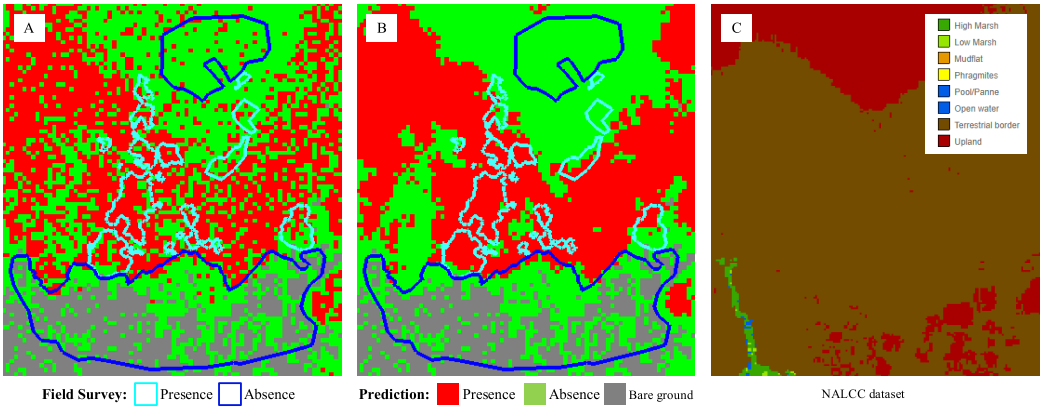

Fig. 8. Enhancing classification accuracy within the Brownsville data through smoothing. (a) Classification results without smoothing; (b) Classification results with four rounds of smoothing; (c) NALCC dataset.

3.4.Robustness of the pipeline

To test the robustness of the *P. australis* classification algorithm, we applied the optimized algorithm from Brownsville to eight distinct sites (Fig. 1) where ground truth data were kept as blind test data to ensure they had no influence on the training phase, neither for pre-classification nor fine-tuning of the classifier. By adopting this approach, we were able to purely evaluate the performance of our proposed pipeline. The optimized algorithm we chose from Brownsville used OM as the feature with 0.5 m height step and a four-round smoothing operation.

The detection algorithm achieved its highest accuracy of 80.65% at Indiantown, while the lowest accuracy of 56.16% was recorded at Howard, both illustrated in Fig. 9. Correspondingly, Indiantown exhibited a recall of 82.61% and an F1-score of 86.36%, whereas Howard demonstrated a recall of 14.00% and an F1-score of 23.93%. Notably, the Virginia sites (Box Tree, Cushman, Indiantown, and Oyster Harbor) generally displayed higher accuracy compared to the Maryland sites. On average, the algorithm in Virginia achieved an Accuracy, Recall, and F1-score of 66.95%, 67.03%, and 58.86%, respectively, while in Maryland, it yielded of 64.44%, 41.25%, and 51.40% (Fig. 9). Classification maps for the eight sites can be found in Fig. 10.

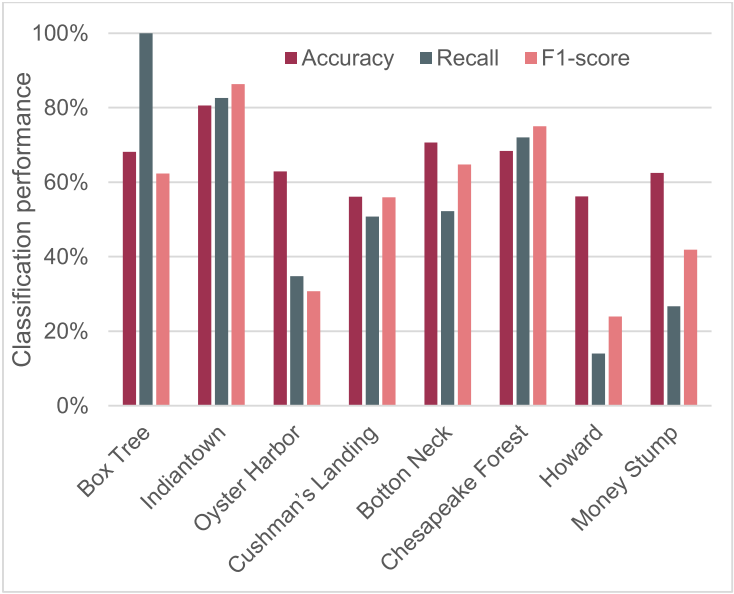

Fig. 9. Detection accuracy across validation sites.

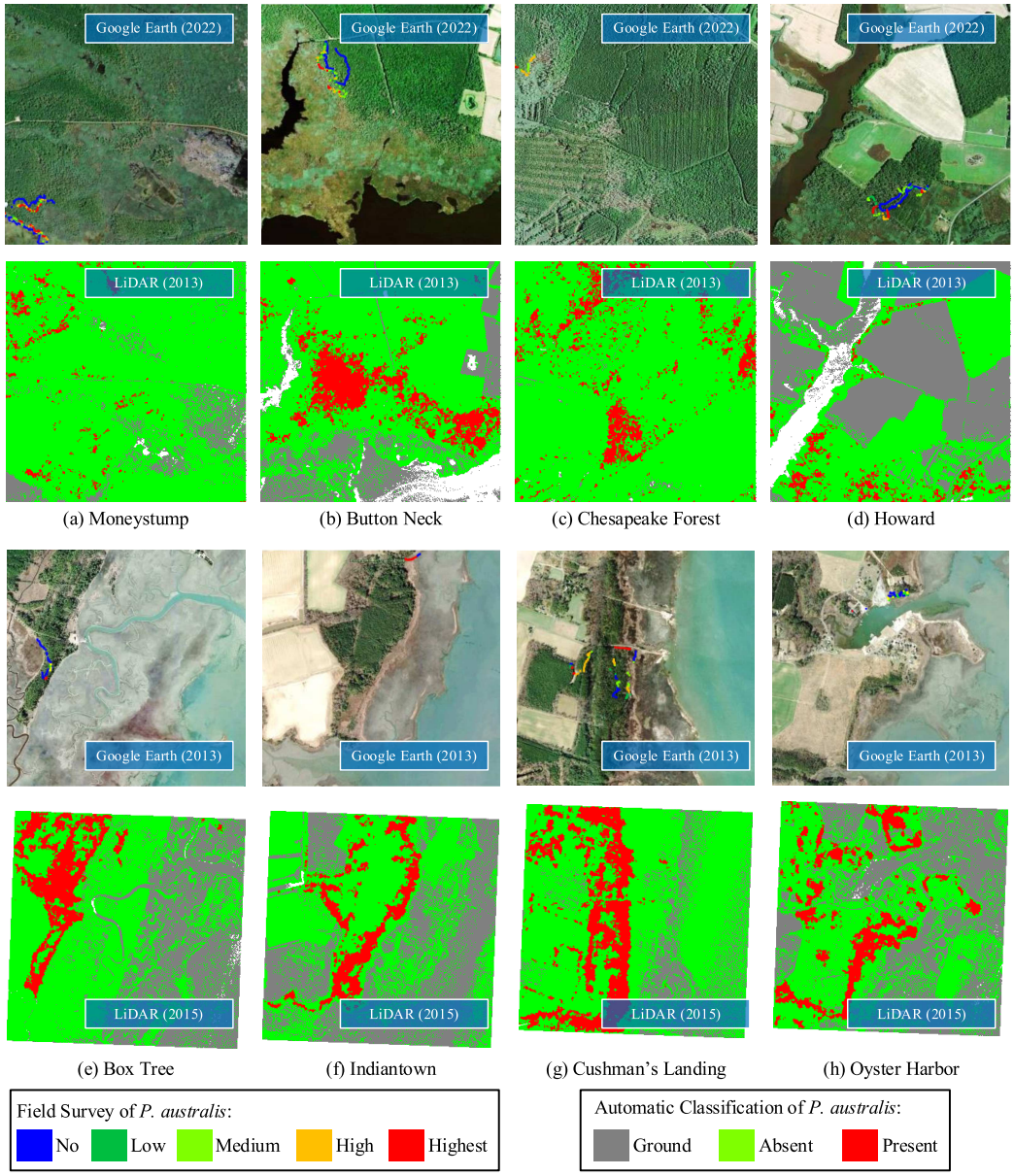

Fig. 10. Detection results at the validation sites. For each site, the top image shows color coded field survey data with stem density on a satellite image from Google Earth, and the bottom image is the *P. australis* distribution map generated by the algorithm that was trained and validated using Brownsville information. Bare ground on the *P. australis* distribution map indicates low-lying areas or water, where *P. australis* is absent.

4. Discussion

In this study, we proposed a *P. australis* detection algorithm using airborne LiDAR data for application

within sea-level-rise-affected coastal areas. We found that metrics representing the spatial distribution of LiDAR points are informative in recognizing species-level plant stands. For *P. australis* specifically, Mean distance, Omnivariance and Eigentropy performed better in *P. australis* detecting than point density and scatter. Detection accuracy reached 91.48% at the most heavily sampled site, where the algorithm was trained, and it reached accuracy of 56.16% to 80.65% at other sites with no training data.

The *P. australis* detection pipeline that we developed in this study, utilizing LiDAR technology, offers an effective means of detecting *P.* australis beneath tree canopies. This innovative technique provides a cost-efficient solution for land managers to identify newly established *P. australis* in deteriorating forests where tree canopy has not fully opened up. Detecting *P .australis* in its early stages of invasion enables land managers to prioritize control efforts to recently invaded forests, where removal is more manageable and cost-effective. Our *P. australis* detection product outperformed existing *P. australis* detection products, i.e. NALCC, which has very limited *P. australis* mapped. Consequently, the proposed *P. australis* detection techniques facilitate close monitoring of *P. australis* invasion dynamics within the forest understory, enabling timely and targeted control actions where they are most needed. The high efficacy and performance of our method in detecting understory plants at the species level underscores the significant potential of LiDAR data in enhancing ecological resolution for forest monitoring.

Optimal height step

The differences in optimal height steps can be attributed to how each feature captures the characteristics of the point cloud data. Researchers find that the size of space partitioning is an essential parameter for canopy estimation using LiDAR point clouds (Wang et al. 2020, Ross et al. 2022). In our case, the eigen-based features perform well with high height steps (around 1.0 m) because they capture local variation within thin computational units. Conversely, the mean distance metric emphasizes the horizontal point distribution, making it more effective at lower height steps (around 0.2m). As the step increases, the eigen-based feature performs better due to its ability to incorporate more 3D characteristics within each unit, while the mean distance metric's detection capability diminishes.

Meanwhile, the optimal height is also influenced by the morphological features of *P. australis*. Stem height of *P. australis* ranges from 1 m to 4 m depending on the maturity. Invasive *P. australis* leaves is dense and with an average internode length of about 0.3 m (field observation by M. Qi). Within a clonal patch, *P.*

australis stems normally share similar stem height. These morphological features make LiDAR points being mostly intercepted by top leaves or surface canopy and result in vertical variation of point density and mean distance from top leaves to the bottom. Therefore, Eigen-based feature that capture the variations with a 3D cell works better at height step larger than internode length, which is 1.0 m in this study. Mean distance that capture the horizontal point distribution can be more sensitive to different point density/spacing between the surface canopy and lower layers with a smaller height step, which is 0.2 m in our study.

In conclusion, understanding the relationships between the morphological features of P. australis and optimal height steps of each metrics enables us to tailor our analysis and select optimal settings for *P. australis* detection. Moreover, this knowledge can guide feature selection and height step choices in similar vegetation or point cloud analysis tasks.

Combined features or single feature

Our result indicates that the combination of Omnivariance and Mean Distance yields better performance compared to singular feature or other combinations. However, as more features are included in the combination, the classification results deteriorated. The increasing number of features negatively impacts the classification performance, suggesting that Eigentropy, Density and Scatter do not contribute additional valuable information to Omnivariance and Mean Distance, but instead introduce noise to the feature space.

Based on these findings, we highly recommend using the OM combination (Omnivariance & Mean Distance) for *P. australis* identification, as it yields superior results compared to other combinations. The OM combination strikes the right balance between accuracy, recall, and F1-score, making it the most suitable choice for effectively identifying *P. australis*. The recommended height step for the OM is 0.5 m, which balanced optimal performance in Accuracy, Recall and F1-score.

Smoothing

The smoothing method we proposed effectively enhanced the detection accuracy of *P. australis* (see Fig. 8). Particularly noteworthy is the considerable reduction in mistakenly detected *P. australis* clusters in thick forest in the Brownsville region (Fig. 8). However, it is worthwhile to mention that excessive smoothing can lead to over-optimization. Fig. 7 shows the smoothing operation achieves the best result after three to four rounds smoothing and decrease with more rounds of smoothing. Therefore, maintaining an appropriate balance in the number of smoothing rounds is crucial to achieving optimal results.

Robustness

When applying the *P. australis* detection algorithm to the validation sites, we observed a decline in detection accuracy from 91.48% to between 80.65 and 56.16% (average of 64%). Several reasons might have contributed to this, namely, regional variation in forest structure, differences in LiDAR data quality, and the lag time between LiDAR data and ground truth data collection. Firstly, spatial heterogeneity in tree canopy and understory LiDAR points characteristics might exist but not have been accounted for in the algorithm developed at Brownsville. Secondly, differences in LiDAR data quality may have played a role. The LiDAR data in Maryland was collected two years earlier than that of Virginia and had a higher point spacing and a smaller number of returns, which is consistent with the generally higher accuracy of the algorithm at the Virginia sites. Thirdly, the time lag between LiDAR and ground truth data collection at the validation sites (i.e. 7 to 9 yrs) was higher than at Brownsville (i.e. 4 yrs), which added uncertainty into classification and introduced potential inconsistencies across sites. in the match of ground truth and LiDAR data, a problem which is inevitable to a greater or lesser degree. However, we recommend minimizing the time difference between ground truth and LiDAR data collection in future studies.

Accuracy

The detection accuracy in our training site achieved 91.48%, which is remarkably high, based on other existing LiDAR-based understory (functional group or species) plant detection efforts , which typically yield accuracies between 40% and 80% (Singh et al. 2015, Latifi et al. 2017, Gopalakrishnan et al. 2018, Hakkenberg et al. 2018). Alhough LiDAR based understory detection efforts have lower accuracy compared with traditional spectral-based methods (Tian et al 2020, Zhang et al 2020, Chen and Shi 2023), traditional spectral based detection are incapable of mapping plant species or functional groups in the forest understory environments. LiDAR-based methods fill this gap, where understory plant distribution mapping was previously impossible. As current *P. australis* mapping products, i.e., NALCC, are incapable of mapping *P. australis* in the forest understory (Fig. 8c), the proposed method provides the first scalable description of *P. australis* distribution in the forest understory.

P. australis distribution pattern

Across all field sites in our study, we found *P. australis* presented typically in low-lying marshes, seaward side of forests with either thin or thick tree canopies (Fig. 8, Fig. 9a,b,d,e, f, h), and forest pocket

(Fig. 9c,g). The presence of *P. australis* in marshes, forest pockets, and thin forests might because *P. australis* prefers high light conditions (Galinato and Van der Valk 1986, Gucker 2008). The presence of *P. australis* beneath dense forests indicates its capability to thrive in low-light environments, a finding corroborated by Shaw et al.'s (2022) field and laboratory-based research. This underscores the pressing need for early monitoring of *P. australis* within forested areas.

Potential applications

This study represents the first successful attempt at detecting *P. australis* beneath forest canopies. With the availability of nationwide airborne LiDAR in United States of America, the method we proposed can be leveraged to a broader scale to generate *P. australis* distribution maps and to facilitate *P. australis* control and forest management.

Additionally, LiDAR data has historically been collected every 5-6 years. Historical LiDAR data provide a unique method to map *P. australis* coverage through time. The historical reconstruction of *P. australis* distribution would provide new information about this cosmopolitan invasive species, such as its expansion rates through time, and provide fundamental insight on the factors that influence *P. australis'* growth and spread.

While the training and evaluation datasets are limited due to the time difference in ground truth and remote sensing data collection, our straightforward classification framework has demonstrated remarkable efficacy and can be reapplied to different data sources, time periods, and environmental contexts. It will serve as a strong foundation for evaluating more intricate methods. Moreover, this integration of data sources opens opportunities to develop new and more complex toolkits for classification, such as the application of Deep Learning on 3D points.

5. Conclusion

In this paper, we propose a novel pipeline specifically designed to detect *P. australis* using publicly-available airborne LiDAR points, particularly in marsh-forest ecotones where the plant is often obscured by tree canopies. We find that the combination of Omnivariance and Mean Distance yield the best results with a 0.5 m height step and four rounds of smoothing. The overall classification accuracy reaches 91.48% in the

training dataset and 56.16% to 80.65% in the validation dataset, enabling us to effectively identify the presence of *P. australis* beneath forest canopies, where *P. australis* could not be detected by current *P. australis* mapping products.

Our proposed algorithm offers a cost-effective means to map *P. australis* using open access airborne LiDAR data nationwide in the United States, which is collected every five to eight years. The generalization of this algorithm could provide distribution maps that would greatly inform local and nationwide conservation and management of native marsh ecosystems. Accelerating sea level rise is increasing the pace of *P. australis* into retreating coastal forests (Smith 2013, Shaw et al. 2022). Our proposed method allows early detection- even under a forested canopy- enabling land managers to intervene prior to full establishment of *P. australis* and the resulting displacement of native marsh species.

Competing interests statement

The authors has no competing interests.

Acknowledgements

This publication was prepared by M. Qi and K. Gedan with support from award F12AP01037 from the US Department of the Interior/US Fish and Wildlife Service to Maryland Sea Grant, the administrative entity for the Mid-Atlantic Panel on Aquatic Invasive Species. Additional funding was provided by, Natural Science Foundation award of Hubei Province of China 2023AFB460, US National Science Foundation awards 2012670 and 1832221. The statements, findings, conclusions, and recommendations are those of the authors and do not necessarily reflect the views of Maryland Sea Grant, the US Department of Interior, or the US Fish and Wildlife Service. The authors thank Jessica MacGregor, Justus Jobe, Aliya Khan, and Riley Leff for contributing field survey data.

References

Anderson, C. J., D. Heins, K. C. Pelletier, and J. F. Knight. 2023. Using Voting-Based Ensemble Classifiers to Map Invasive Phragmites australis. Remote Sensing.

Axelsson, P. 2000. DEM generation from laser scanner data using adaptive TIN models. International archives of photogrammetry and remote sensing **33**:110-117.

Bazezew, M. N., Y. A. Hussin, E. H. Kloosterman, I. M. M. Hasmadi, T. Soromessa, and M. S. Adan. 2021. Factual approach for tropical forest parameters measurement and monitoring: future option with a focus on synergetic use of airborne and terrestrial LiDAR technologies. INTERNATIONAL JOURNAL OF REMOTE SENSING **42**:3219-3230.

Campbell, M. J., P. E. Dennison, A. T. Hudak, L. M. Parham, and B. W. Butler. 2018. Quantifying understory vegetation density using small-footprint airborne lidar. Remote Sensing of Environment **215**:330-342.

Cassalho, F., A. de S. de Lima, C. M. Ferreira, M. Henke, G. de A. Coelho, T. W. Miesse, J. Johnston, D. J. Coleman. 2023. Quantifying the effects of sea level rise driven marsh migration on wave attenuation. Environmental Monitoring and Assessment **195**(12): 1487.

Chen, W., and C. Shi. 2023. Fine-scale mapping of Spartina alterniflora-invaded mangrove forests with multi-temporal WorldView-Sentinel-2 data fusion. Remote Sensing of Environment **295**:113690.

Chen, Y., and M. L. Kirwan. 2022. A phenology-and trend-based approach for accurate mapping of sea-level driven coastal forest retreat. Remote Sensing of Environment **281**:113229.

Coleman, D. J., M. Schuerch, S. Temmerman, G. Guntenspergen, C. G. Smith, and M. L. Kirwan. 2022. Reconciling models and measurements of marsh vulnerability to sea level rise. Limnology and Oceanography Letters **7**:140-149.

Dai, J., D. A. Roberts, D. A. Stow, L. An, S. J. Hall, S. T. Yabiku, and P. C. Kyriakidis. 2020. Mapping understory invasive plant species with field and remotely sensed data in Chitwan, Nepal. Remote Sensing of Environment **250**:112037.

de Almeida, D. R. A., E. N. Broadbent, M. P. Ferreira, P. Meli, A. M. A. Zambrano, E. B. Gorgens, A. F. Resende, C. T. de Almeida, C. H. do Amaral, A. P. D. Corte, C. A. Silva, J. P. Romanelli, G. A. Prata, D. d. A. Papa, S. C. Stark, R. Valbuena, B. W. Nelsonn, J. Guillemot, J.-B. Feret, R. Chazdon, and P. H. S. Brancalion. 2021. Monitoring restored tropical forest diversity and structure through UAV-borne hyperspectral and lidar fusion. Remote Sensing of Environment **264**.

Galinato, M.I., and A.G. Van der Valk. 1986. Seed germination traits of annuals and emergents recruited during drawdowns in the Delta Marsh, Manitoba, Canada. Aquatic Botany **26**: 89–102.

Gedan, K. B., and E. Fernández-Pascual. 2019. Salt marsh migration into salinized agricultural fields: A novel assembly of plant communities. Journal of Vegetation Science **30**:1007-1016.

Gopalakrishnan, R., V. A. Thomas, R. H. Wynne, J. W. Coulston, and T. R. Fox. 2018. Shrub detection using disparate airborne laser scanning acquisitions over varied forest cover types. International Journal of Remote

Sensing **39**:1220-1242.

Gucker, C. L. 2008. Phragmites australis. U.S. Department of Agriculture, Forest Service, Rocky Mountain Research Station, Fire Sciences Laboratory. Fire Effects Information System.

Hakkenberg, C. R., K. Zhu, R. K. Peet, and C. Song. 2018. Mapping multi-scale vascular plant richness in a forest landscape with integrated LiDAR and hyperspectral remote-sensing. Ecology **99**:474-487.

Hazelton, E. L., T. J. Mozdzer, D. M. Burdick, K. M. Kettenring, and D. F. Whigham. 2014. Phragmites australis management in the United States: 40 years of methods and outcomes. AoB plants **6**.

Huo, L., E. Lindberg, and J. Holmgren. 2022. Towards low vegetation identification: A new method for tree crown segmentation from LiDAR data based on a symmetrical structure detection algorithm (SSD). Remote Sensing of Environment **270**:112857.

Jucker, T., C. R. Gosper, G. Wiehl, P. B. Yeoh, N. Raisbeck-Brown, F. J. Fischer, J. Graham, H. Langley, W. Newchurch, and A. J. O'Donnell. 2023. Using multi-platform LiDAR to guide the conservation of the world's largest temperate woodland. Remote Sensing of Environment **296**:113745.

Karen, F. W., N. W. Brian, R. L. James, P. Steven, M. T. Joseph, and A. E. Iverson. 2004. Context-driven automated target detection in 3D data. Pages 133-143 *in* Proc.SPIE.

Kearney, W. S., A. Fernandes, and S. Fagherazzi. 2019. Sea-level rise and storm surges structure coastal forests into persistence and regeneration niches. PLOS ONE **14**:e0215977.

Kettenring, K. M., K. E. Mock, B. Zaman, and M. McKee. 2016. Life on the edge: reproductive mode and rate of invasive Phragmites australis patch expansion. Biological Invasions **18**:2475-2495.

Kirwan, M. L., and K. B. Gedan. 2019. Sea-level driven land conversion and the formation of ghost forests. Nature Climate Change **9**:450-457.

Kostensalo, J., L. Mehtätalo, S. Tuominen, P. Packalen, and M. Myllymäki. 2023. Recreating structurally realistic tree maps with airborne laser scanning and ground measurements. Remote Sensing of Environment **298**:113782.

Kottler, E. J., and K. Gedan. 2020. Seeds of change: characterizing the soil seed bank of a migrating salt marsh. Annals of Botany **125**:335-344.

Langston, A. K., D. J. Coleman, N. W. Jung, J. L. Shawler, A. J. Smith, B. L. Williams, S. S. Wittyngham, R. M. Chambers, J. E. Perry, and M. L. Kirwan. 2022. The effect of marsh age on ecosystem function in a rapidly transgressing marsh. Ecosystems **25**:252-264.

Latifi, H., M. Heurich, F. Hartig, J. Müller, P. Krzystek, H. Jehl, and S. Dech. 2016. Estimating over- and

understorey canopy density of temperate mixed stands by airborne LiDAR data. Forestry: An International Journal of Forest Research **89**:69-81.

Latifi, H., S. Hill, B. Schumann, M. Heurich, and S. Dech. 2017. Multi-model estimation of understorey shrub, herb and moss cover in temperate forest stands by laser scanner data. Forestry: An International Journal of Forest Research **90**:496-514.

Li, S., T. Wang, Z. Hou, Y. Gong, L. Feng, and J. Ge. 2021. Harnessing terrestrial laser scanning to predict understory biomass in temperate mixed forests. Ecological Indicators **121**.

Lines, E. R., F. J. Fischer, H. J. F. Owen, and T. Jucker. 2022. The shape of trees: Reimagining forest ecology in three dimensions with remote sensing. Journal of Ecology **110**:1730-1745.

Martin, L. J., and B. Blossey. 2013. The Runaway Weed: Costs and Failures of Phragmites australis Management in the USA. Estuaries and Coasts **36**:626-632.

Melo, A. M., C. R. Reis, B. F. Martins, T. M. A. Penido, L. C. E. Rodriguez, and E. B. Gorgens. 2021. Monitoring the understory in eucalyptus plantations using airborne laser scanning. SCIENTIA AGRICOLA **78**.

Meyerson, L. A., K. Saltonstall, L. Windham, E. Kiviat, and S. Findlay. 2000. A comparison of Phragmites australisin freshwater and brackish marsh environments in North America. Wetlands Ecology and Management **8**:89-103.

Rooth, J. E., and J. C. Stevenson. 2000. Sediment deposition patterns in Phragmites australiscommunities: Implications for coastal areas threatened by rising sea-level. Wetlands Ecology and Management **8**:173-183.

Ross, C. W., E. L. Loudermilk, N. Skowronski, S. Pokswinski, J. K. Hiers, and J. O'Brien. 2022. LiDAR voxel-size optimization for canopy gap estimation. Remote Sensing **14**:1054.

Saltonstall, K. 2002. Cryptic invasion by a non-native genotype of the common reed, Phragmites australis, into North America. Proceedings of the National Academy of Sciences **99**:2445-2449.

Saltonstall, K., and L. A. Meyerson. 2016. Phragmites australis: from genes to ecosystems. Biological Invasions **18**:2415-2420.

Shaw, P., J. Jobe, and K. B. Gedan. 2022. Environmental Limits on the Spread of Invasive Phragmites australis into Upland Forests with Marine Transgression. Estuaries and Coasts **45**:539-550.

Singh, K. K., A. J. Davis, and R. K. Meentemeyer. 2015. Detecting understory plant invasion in urban forests using LiDAR. International Journal of Applied Earth Observation and Geoinformation **38**:267-279.

Smith, J. A. M. 2013. The Role of Phragmites australis in Mediating Inland Salt Marsh Migration in a Mid-Atlantic Estuary. Plos One **8**:e65091.

585 Song, J., X. Zhu, J. Qi, Y. Pang, L. Yang, and L. Yu. 2021. A Method for Quantifying Understory Leaf Area Index
586 in a Temperate Forest through Combining Small Footprint Full-Waveform and Point Cloud LiDAR Data.
587 Remote Sensing **13**.
588 Sumnall, M. J., A. Trlica, D. R. Carter, R. L. Cook, M. L. Schulte, O. C. Campoe, R. A. Rubilar, R. H. Wynne,
589 and V. A. Thomas. 2021. Estimating the overstory and understory vertical extents and their leaf area index in
590 intensively managed loblolly pine (Pinus taeda L.) plantations using airborne laser scanning. Remote Sensing
591 of Environment **254**.
592 Sward, R., A. Philbrick, J. Morreale, C. J. Baird, and K. Gedan. 2023. Shrub expansion in maritime forest
593 responding to sea level rise. Frontiers in Forests and Global Change **6**.
594 Thompson, J. A. 2003. Common reed (Phragmites australis) in the Chesapeake Bay: a draft bay-wide management
595 plan.*in* U. S. F. a. W. Service, editor., http://www.midatlanticpanel.org/wp-
596 content/uploads/2016/04/phragmites_102003.pdf.
597 Tian, J., L. Wang, D. Yin, X. Li, C. Diao, H. Gong, C. Shi, M. Menenti, Y. Ge, S. Nie, Y. Ou, X. Song, and X.
598 Liu. 2020. Development of spectral-phenological features for deep learning to understand Spartina
599 alterniflora invasion. Remote Sensing of Environment **242**:111745.
600 Torralba, J., P. Crespo-Peremarch, and L. A. Ruiz. 2018. Assessing the use of discrete, full-waveform LiDAR and
601 TLS to classify Mediterranean forest species composition. REVISTA DE TELEDETECCION:27-40.
602 Venier, L. A., T. Swystun, M. J. Mazerolle, D. P. Kreutzweiser, K. L. Wainio-Keizer, K. A. McIlwrick, M. E.
603 Woods, and X. Wang. 2019. Modelling vegetation understory cover using LiDAR metrics. PLOS ONE **14**.
604 Walter, M., and P. Mondal. 2023. Mapping of Phragmites in estuarine wetlands using high-resolution aerial
605 imagery. Environmental Monitoring and Assessment **195**:478.
606 Wang, C., S. Luo, X. Xi, S. Nie, D. Ma, and Y. Huang. 2020. Influence of voxel size on forest canopy height
607 estimates using full-waveform airborne LiDAR data. Forest Ecosystems **7**:1-12.
608 Wilen, B. O., and M. Bates. 1995. The US fish and wildlife service's national wetlands inventory project.
609 Classification and inventory of the world's wetlands:153-169.
610 Windham, L. 2001. Comparison of biomass production and decomposition between Phragmites australis
611 (Common Reed) and Spartina patens (Salt Hay Grass) in brackish tidal marshes of New Jersey. Wetlands
612 **21**:179-188.
613 Zhang, X., X. Xiao, X. Wang, X. Xu, B. Chen, J. Wang, J. Ma, B. Zhao, and B. Li. 2020. Quantifying expansion
614 and removal of Spartina alterniflora on Chongming island, China, using time series Landsat images during

1995-2018. Remote Sensing of Environment **247**:111916.

Appendix A

Table A1 Imagery of species typical to the marsh-forest ecotone

Plant species	Habitat	True color drone images
Phragmites australis	Marsh	 (11.2 × 11.2 m)
Juncus roemerianus	Marsh	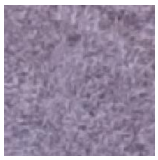 (11.2 × 11.2 m)
Spartina patens & *Distichlis spicata* mixed stands	Marsh	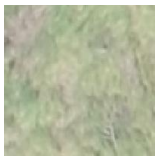 (11.2 × 11.2 m)
Tree canopies	Transitional forest	 (28 × 28 m)
Phragmites australis (outline in red) in a tree canopy gap	Transitional forest	 (28 × 28 m)

Declaration of interests

☒The authors declare that they have no known competing financial interests or personal relationships that could have appeared to influence the work reported in this paper.

☐The authors declare the following financial interests/personal relationships which may be considered as potential competing interests: